PAPER

Synergistic design of g-C₃N₄-supported CNTs: experimental and DFT insights for enhanced electrochemical performance in flexible Li–S batteries†

Vijay K. Tomer, [ID] *[a] Rameshwar L. Kumawat, [ID] [b] Otavio Augusto Titton Dias,[a] Ritu Malik, [ID] *[a] George C. Schatz [ID] [b] and Mohini Sain[a]

In addressing the shuttle effect and sluggish redox kinetics of lithium polysulfides (LiPSs) in lithium–sulfur batteries, we developed a novel heterostructure combining 1D carbon nanotubes (CNTs) grown on a 2D sheet of graphitic carbon nitride (g-C₃N₄) to improve conversion reaction kinetics and LiPS adsorption capacity. The high pyridine N content in g-C₃N₄ facilitates homogeneous Li ion deposition and enhances affinity between Li and N atoms. Extensive experimental characterization and density functional theory (DFT) calculations validated the interaction between g-C₃N₄-CNT/S and LiPSs. In pouch cell evaluation, the hybrid g-C₃N₄-CNT/S cathode, with ∼70% sulfur loading, demonstrated outstanding rate performance, delivering ∼895 mA h g⁻¹ at 0.1C and retaining ∼500 mA h g⁻¹ even at 1.5C under lean electrolyte conditions (E/S ∼5 μl mg⁻¹). Long-term stability over 250 cycles, with a capacity retention of 86% and a coulombic efficiency (CE) of 90.4%, was achieved, even with an elevated sulfur loading of 6.2 mg cm⁻². Post-mortem investigation using X-ray photoelectron spectroscopy (XPS) and electrochemical impedance spectroscopy (EIS) elucidated surface chemistry changes and elemental composition alterations, highlighting the formation of various reaction products during charge–discharge cycles. This study underscores the cost-effective heterostructure strategy's potential for advancing LiSBs in practical applications.

Introduction

Developing reliable energy storage and conversion technologies is essential in the face of the growing energy crisis and climate change.[1,2] Meeting the increasing demand for portable electronic devices and electric vehicles necessitates advanced, affordable, lightweight, and durable rechargeable batteries.[3] Lithium-ion batteries (LIBs) have long been favored because of their high power/energy density and extended service life, making them promising for various applications.[4,5] However, conventional LIBs are nearing their theoretical energy density limits and cannot keep up with escalating energy demands.[6] As a potential solution, lithium–sulfur batteries (LiSBs) offer significant cost reduction and a substantial boost in energy density, approximately 2600 W h kg⁻¹, three to five times higher than that of commercial LIBs based on intercalation reactions.[7,8] Sulfur, a low-cost and abundant cathode material, further enhances the appeal of LiSBs, showcasing advantages for large-scale applications compared to traditional LIB cathode materials such as LiFePO₄, LiMn₂O₄, LiCoO₂, *etc.*[9] Despite these advantages, LiSBs face challenges such as rapid capacity loss and low coulombic efficiency (CE), hindering their commercialization.[10] The poor conductivity of sulfur and its lithiation products (Li₂S/Li₂S₂) results in sluggish reaction kinetics, leading to issues during charge–discharge cycles.[11] Soluble lithium polysulfides (LiPSs) formed as reaction intermediates contribute to irreversible capacity loss, low CE, and Li anode corrosion.[12] Additionally, the substantial volume expansion (∼80%) during cycling causes structural collapse and significantly reduces cathode activity.[13] Addressing these challenges requires the design of suitable S-hosting materials to enhance cathode conductivity and limit polysulfide dissolution.

Recently, cathode hosts with strong physical and chemical interactions toward LiPSs have improved capacity retention by suppressing the shuttle phenomenon and improving redox kinetics.[13,14] A template-based method was employed to synthesize a composite host of macro/mesoporous carbon and

[a]Department of Mechanical & Industrial Engineering, University of Toronto, Toronto, Canada. E-mail: vj.kumar@utoronto.ca; ritu.kumar@utoronto.ca

[b]Department of Chemistry, Northwestern University, Illinois, USA

† Electronic supplementary information (ESI) available: Gibbs free energy of the sulfur reduction reaction (SRR); tables illustrating bandgap and binding energy values for S₈/LiPSs calculated from DFT analysis, electrochemical performance comparison with previously published studies; BET sorption isotherms; TGA; CV cycling performance; complete XPS scan and EIS spectra for the cycled cell. See DOI: https://doi.org/10.1039/d4ta00918e

defective TiO_2 nanoparticles, showcasing a high capacity (1420 mA h g^{-1} at 0.2C) and cycling ability (65.6% retention at 0.2C over 60 cycles).[15] Additionally, tin disulfide (SnS_2) nanosheets were anchored onto nitrogen-doped hollow carbon with mesoporous shells, forming a bipolar dynamic host with a capacity of 947.4 mA h g^{-1} at 0.2C.[16] Among the various host matrices explored in the past few years,[17–19] graphitic carbon nitride (g-C_3N_4 or g-CN), a semiconductor material with a 2D structure akin to graphene, exhibits promising potential for improving Li–S battery performance.[20] Recent studies highlight g-C_3N_4's catalytic activity, stability, cost-effectiveness, and environmental friendliness, making it an attractive additive for Li–S batteries. The heptazine units in g-C_3N_4, containing high levels of pyridinic N, enable homogenized Li ion deposition and a strong affinity between Li and N atoms.[21,22] Benefiting from the inherent high charge polarity and abundant polysulfide binding site, g-C_3N_4 manifested remarkable electrocatalytic performance toward converting polysulfides during the charge/discharge process in LiSBs.[23] Novel approaches, such as nitrogen-deficient g-C_3N_4 heterostructures developed through magnesiothermic denitriding technology,[24] have demonstrated significant improvements. These structures achieved a discharge capacity of 650 mA h g^{-1} at 4C with low-capacity decay after 400 cycles. Similarly, g-C_3N_4/g-C_3N_4 heterojunctions[25] adjusted the electron cloud structure, providing an initial discharge capacity of 1200 mA h g^{-1} and maintaining 464 mA h g^{-1} after 150 cycles. Other techniques, like the ethanol-assisted spray drying method, produced rGO/g-C_3N_4/CNT microspheres,[26] offering enhanced electrode conductivity and stable cycling performance. 3D porous graphene@g-C_3N_4 hybrid sponges,[27] as sulfur host materials, exhibited high specific capacity and excellent rate capability, thanks to their porous network structure. While these examples showcase g-C_3N_4's effectiveness as a sulfur host, many strategies have simply mixed carbon materials and g-C_3N_4 without considering their mutual impact. Consequently, there is a pressing need for a simple, efficient, and low-cost synthesis technique to produce a network structure hybrid with superior Li–S battery performance.

Leveraging a cost-effective melamine precursor and a straightforward pyrolysis process, we synthesized low-cost 2D sheet-like nitrogen-rich g-C_3N_4 and composited it with multi-walled 1D CNTs to form a heterostructure. This design not only accommodates sulfur volume expansion during lithiation but also acts as a physical barrier, preventing polysulfide diffusion from the cathode. The enriched N-sites in g-C_3N_4 serve as adhesion sites for polysulfides, establishing a 'physical–chemical' dual-confinement for enhanced confinement.[20] The interlinked hierarchical network of 1D CNTs on 2D g-C_3N_4 promotes rapid electron/Li$^+$ transport and structural integrity, ensuring swift reaction kinetics and long-term cycling stability. The g-C_3N_4-CNT/S composite exhibits outstanding performance, demonstrating a high specific capacity and exceptional cycling stability with a mere 0.053% capacity decay per cycle over 250 cycles and an impressive capacity retention of 90.4% at a 0.1C rate. Notably, the pouch cell has no sign of performance decay even at a folding angle of 180°, showcasing its potential for practical applications.

Experimental section

Materials

Melamine (99.99%), *N*-methyl-2-pyrrolidone (NMP), lithium bis(trifluoromethane) sulfonimide (LiTFSI), 1,3-dioxolane (DOL), 1,2-dimethoxyethane (DME) and lithium nitrate ($LiNO_3$) were purchased from Sigma. Conducting carbon (CC, Super C45), polyvinylidene fluoride (PVDF) as the binder, Al foil (cathode current collector), Cu foil (anode current collector), a tri-layered (PP/PE/PP) 25 μm thick separator (Celgard 2325), and tabs (Al and Ni) were purchased from MTI (USA). Pure lithium foil (100 μm) as an anode, lithium sulfide (Li_2S 99.99%), and CNTs (multi-walled) were purchased from Nanochemazone (Canada). All the materials were used as received without further treatment.

Synthesis of cathode active materials

g-C_3N_4 powder was synthesized *via* thermal polymerization of melamine. In a typical process, the melamine (5 g) was heated to 600 °C at a ramp rate of 5 °C min^{-1} for 4 h in a covered ceramic crucible. After cooling to room temperature, the resulting light-yellow solid was ground to yield bulk g-C_3N_4 powder, which was further dispersed in deionized water (90 mL) and sonicated for 4 h to obtain delaminated g-C_3N_4 NSs. The g-C_3N_4 and CNTs (in a 2 : 3 weight ratio) were combined in a glass vial with 20 mL of deionized water and sonicated for 4 h. The resulting product was filtered and dried at 60 °C overnight, yielding g-C_3N_4-CNT. For sulfur-based composites, pure g-C_3N_4 and g-C_3N_4-CNT composites were individually ground with sulfur (3 : 7 weight ratio) for 1 h and heated at 160 °C for 15 h to produce g-C_3N_4/S and g-C_3N_4-CNT/S composites, respectively (Scheme 1).

Material characterization

Crystalline structures were analyzed using a Philips P.W. 1830 powder X-ray diffractometer with a CuKα-ray source (10–70° scan range). The microstructure and morphology were examined with a JEOL 2010 transmission electron microscope and QUANTA FEG 250 scanning electron microscope equipped with an energy-dispersive X-ray spectrometer (EDS). Fourier Transform Infrared (FTIR) spectroscopy was performed from 500 to 4000 cm^{-1} on a Tensor 27 instrument. Carbon defects were assessed using Raman spectroscopy (Bruker Senterra Infinity 1). The chemical and electronic states of the surface were investigated *via* X-ray photoelectron spectroscopy (XPS, PerkinElmer Phi 5500 ESCA spectrophotometer). The Brunauer–Emmett–Teller (BET) surface area and pore size were determined by N_2 adsorption/desorption measurements (Quantachrome Nova 1200 Analyzer) after degassing the sample under vacuum at 150 °C for 2 h. The sulfur content in composite materials was measured by thermogravimetric differential scanning calorimetry (TGA, Q50) with a 5 °C min^{-1} heating rate from 25 to 600 °C.

This journal is © The Royal Society of Chemistry 2024

J. Mater. Chem. A, 2024, **12**, 15814–15828 | **15815**
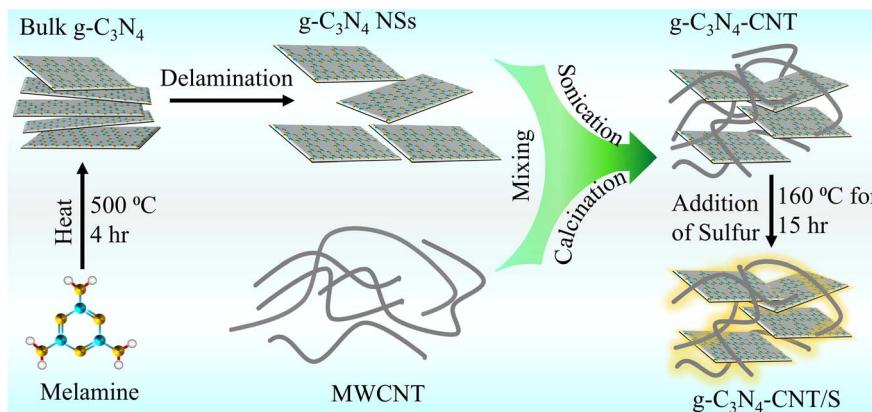
Scheme 1 Schematic illustration for the synthesis of the g-C$_3$N$_4$-CNT/S nanocomposite.

Conductivity measurements were performed on sheets (10 × 20 mm) using the Ossila four-point probe technique.

Lithium–sulfur battery assembly

Slurry preparation. The cathode slurry comprised 80 wt% active materials (AM: g-C$_3$N$_4$/S or g-C$_3$N$_4$-CNT/S), 10 wt% conducting carbon (CC: Super C45), and 10 wt% PVDF binder in NMP. For slurry preparation, 4 g AM was ball-milled with 0.5 g CC for 30 minutes at 500 rpm. Simultaneously, 0.5 g PVDF was mixed with 5 mL NMP at 50 °C until a transparent viscous solution formed. The pre-mixed AM/CC was gradually added to this viscous solution in several batches, creating a uniform slurry that was stirred overnight at 40 °C. The slurry underwent homogenization using a dual-shaft planetary mixer under vacuum for 30 minutes to eliminate trapped air bubbles.

Electrode preparation. The wet slurry was coated onto Al foil using a tape casting machine with a 10 cm long doctor blade at a low coating speed of 6 mm s^{-1}, followed by overnight vacuum drying at 60 °C. The resulting dried sheet underwent calendaring to enhance tap density and eliminate vulnerable pores. Using a semi-automatic slitting machine (MTI, USA), sheets were cut into electrodes measuring 56 mm (l) × 43 mm (w) with the average areal sulfur loading varying from ∼4–6.5 mg cm^{-2}.

Pouch assembly and cell aging. The single-coated cathode sheets (Scheme 2) were Z-stacked with double-sided metallic Li anode sheets (54 mm (l) × 41 mm (w)) and separated by a trilayer (PP/PE/PP) separator (25 μm thickness, Celgard 2325) in an argon-filled glove box with H$_2$O and O$_2$ contents below 0.1 ppm. The electrolyte, comprising 1 M LiTFSI and 2 wt% LiNO$_3$ in a 1 : 1 vol. ratio of 1,3-dioxolane (DOL) and 1,2-dimethoxyethane (DME), had a volume maintained at 5 μL mg^{-1} sulfur. Sealed pouch cells were pressed for 2 h under an Ar atmosphere and then transferred to a vacuum oven for 12 h at 50 °C for aging.

Electrochemical measurements. Galvanostatic charging/discharging profiles for the prepared pouch cells were recorded using an 8 Channel Battery Analyzer (MTI, USA) within a cut-off voltage range of 1.8–2.8 V. Cyclic voltammetry (CV) and electrochemical impedance spectroscopy (EIS) were performed on an Admiral Instruments Squidstat Plus potentiostat. CV plots covered a potential range of 1.6–2.8 V with a scan rate varying from 0.05 to 1 mV s^{-1}. EIS curves were obtained under open circuit potential, in a frequency range of 2 mHz–0.5 Hz, at an excitation potential of 10 mV, and 20 points per decade.

Polysulfide adsorption tests

The absorption behaviors of active materials towards polysulfides were assessed by immersing them in a Li$_2$S$_6$ solution, chosen as the representative of polysulfides. For Li$_2$S$_6$ solution preparation, Li$_2$S and sulfur powders (1 : 5 molar ratio) were added to a DOL and DME solution (1 : 1, v/v) under vigorous stirring at 60 °C for 24 h in an Ar-filled glovebox. The concentration of the resulting Li$_2$S$_6$ solution was 5 mmol L^{-1}. Before the polysulfide adsorption test, pure g-C$_3$N$_4$ and g-C$_3$N$_4$-CNT hybrids were dried at 60 °C under vacuum for 12 h. Subsequently, g-C$_3$N$_4$ and g-C$_3$N$_4$-CNT hybrids with an equal weight (20 mg) were immersed in a 5 mL Li$_2$S$_6$ solution for static adsorption over 12 h. The color variation of the supernatant over time was observed, and the adsorption capability of g-C$_3$N$_4$ and g-C$_3$N$_4$-CNT to Li$_2$S$_6$ was tested *via* UV-vis spectroscopy. A blank Li$_2$S$_6$ solution served as the reference.

Computational details

The electronic structure calculations used the Vienna *ab initio* Simulation Package (VASP) with projector-augmented wave (PAW) pseudopotentials.[28–30] The Perdew–Burke–Ernzerhof generalized gradient approximation (GGA-PBE) is employed to capture the exchange–correlation potentials.[31] A plane wave cutoff energy of 470 eV was set, enhancing the accuracy of our electronic structure calculations. To address van der Waals (vdW) interactions, the DFT-D3 method developed by Grimme was systematically incorporated into all calculations. The application of the DFT-D3 (ref. 32) method included the use of a zero-damping function, further contributing to the accuracy and reliability of our computational results. The geometry relaxation of all structures is meticulously conducted until the Hellmann–Feynman forces acting on each atom reach a value below 10^{-2} eV Å^{-1}. Simultaneously, total energy convergence is rigorously pursued until it reaches 10^{-4} eV. To adequately

15816 | *J. Mater. Chem. A*, 2024, **12**, 15814–15828

This journal is © The Royal Society of Chemistry 2024
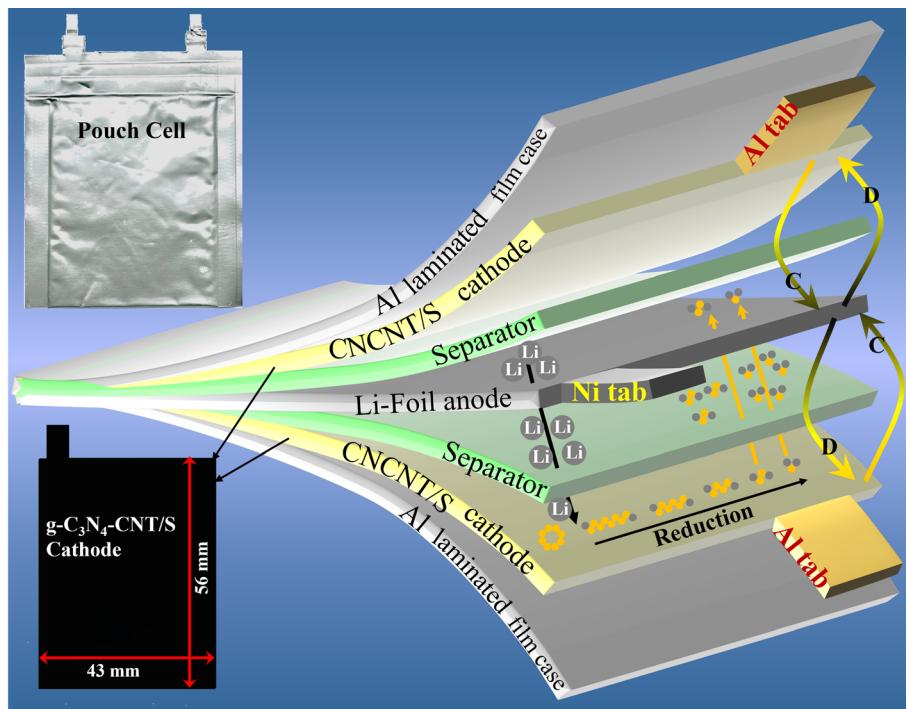
Scheme 2 Schematic for the structure of the pouch cell demonstrating the arrangements of electrodes and separator.

sample the Brillouin zone, a regular Γ-centered k-point mesh is utilized with a grid that is $3 \times 3 \times 1$.[33] The initial optimization involved separate adjustments of the unit cells for the g-C$_3$N$_4$ and CNT surfaces. Subsequently, supercells of dimensions $2 \times 1 \times 1$ are constructed for each system, accompanied by the introduction of a vacuum region of approximately 30 Å around each supercell in the z-direction. LiPSs and S$_8$ molecules are also individually optimized before being placed on the surfaces. Further simulations involved the strategic placement of S$_8$ and LiPS molecules on both g-C$_3$N$_4$ and the heterostructure formed by combining g-C$_3$N$_4$ and CNT (g-C$_3$N$_4$-CNT). A comprehensive relaxation of the S$_8$/LiPSs + g-C$_3$N$_4$ and S$_8$/LiPSs + g-C$_3$N$_4$-CNT configurations is then carried out using the above-mentioned computational parameters.

In the pursuit of identifying the energetically most favorable configurations of S$_8$/LiPSs, we theoretically investigated the adsorption of S$_8$/LiPSs molecules on both g-C$_3$N$_4$ and g-C$_3$N$_4$-CNT surfaces. Our exploration encompassed a thorough examination of various possible orientations and configurations of the S$_8$/LiPS molecules. The energetically most stable configurations for each LiPS and S$_8$ molecule are considered for binding energy studies. The binding energy (E_b in eV) of each LiPS and S$_8$ molecule on the g-C$_3$N$_4$ surface and g-C$_3$N$_4$-CNT composite surface is calculated using the following equation:

$$E_b = E_S + E_{\text{g-C}_3\text{N}_4/\text{g-C}_3\text{N}_4\text{-CNT}} - E_{\text{S+g-C}_3\text{N}_4/\text{g-C}_3\text{N}_4\text{-CNT}} \quad (1)$$

where S = S$_8$/Li$_2$S$_n$ and n = 1, 2, 4, 6, 8. E_S represents the total optimized energies of the isolated S$_8$/Li$_2$S$_n$ molecules, and $E_{\text{g-C}_3\text{N}_4/\text{g-C}_3\text{N}_4\text{-CNT}}$ denotes the total optimized energies of g-C$_3$N$_4$ and g-C$_3$N$_4$-CNT surfaces. $E_{\text{S+g-C}_3\text{N}_4/\text{g-C}_3\text{N}_4\text{-CNT}}$ is the total optimized

energy of the S + g-C$_3$N$_4$ and S + g-C$_3$N$_4$-CNT configurations (*i.e.*, the energetically most favorable configurations).

The Gibbs free energy (ΔG) of the sulfur reduction reaction: the reaction Gibbs free energy of S$_8$ and Li$_2$S$_n$ on g-C$_3$N$_4$ and g-C$_3$N$_4$-CNT composite surfaces was calculated by using the following equation:

$$\Delta G = \Delta E_{\text{dft}} - (\Delta \text{ZPE} + T\Delta S) \quad (2)$$

where ΔE_{dft} represents the difference between products and reactants computed by DFT calculation, ΔZPE and $T\Delta S$ are the difference of the zero-point energy (ZPE) and entropic contribution, respectively. The ΔE_{dft} is obtained from the corresponding VASP computation, while the ZPE, enthalpy, and entropy contributions are computed from vibrational frequency calculations and using the Vaspkit[34] tool at 300 K. A detailed discussion on this can be found in the ESI.†

Results & discussion

Active material characterization

The XRD patterns in Fig. 1a depict the crystalline characteristics of as-prepared g-C$_3$N$_4$, g-C$_3$N$_4$/S, and g-C$_3$N$_4$-CNT/S. Pure g-C$_3$N$_4$ exhibits a low-angle reflection peak at ~13°, indicative of lattice planes parallel to the c-axis.[35,36] Additional peaks at 27.9° result from the periodic stacking of heptazine layers in the nanosheets.[37,38] In the g-C$_3$N$_4$-CNT/S spectrum, peaks at 26.3° and 42.7° correspond to the hexagonal graphite structure in CNTs along the (002) and (100) directions.[39] The well-aligned diffraction peaks of the orthorhombic sulfur phase (JCPDS card no. 08-0247) in both g-C$_3$N$_4$/S and g-C$_3$N$_4$-CNT/S confirm the

This journal is © The Royal Society of Chemistry 2024

J. Mater. Chem. A, 2024, **12**, 15814–15828 | **15817**
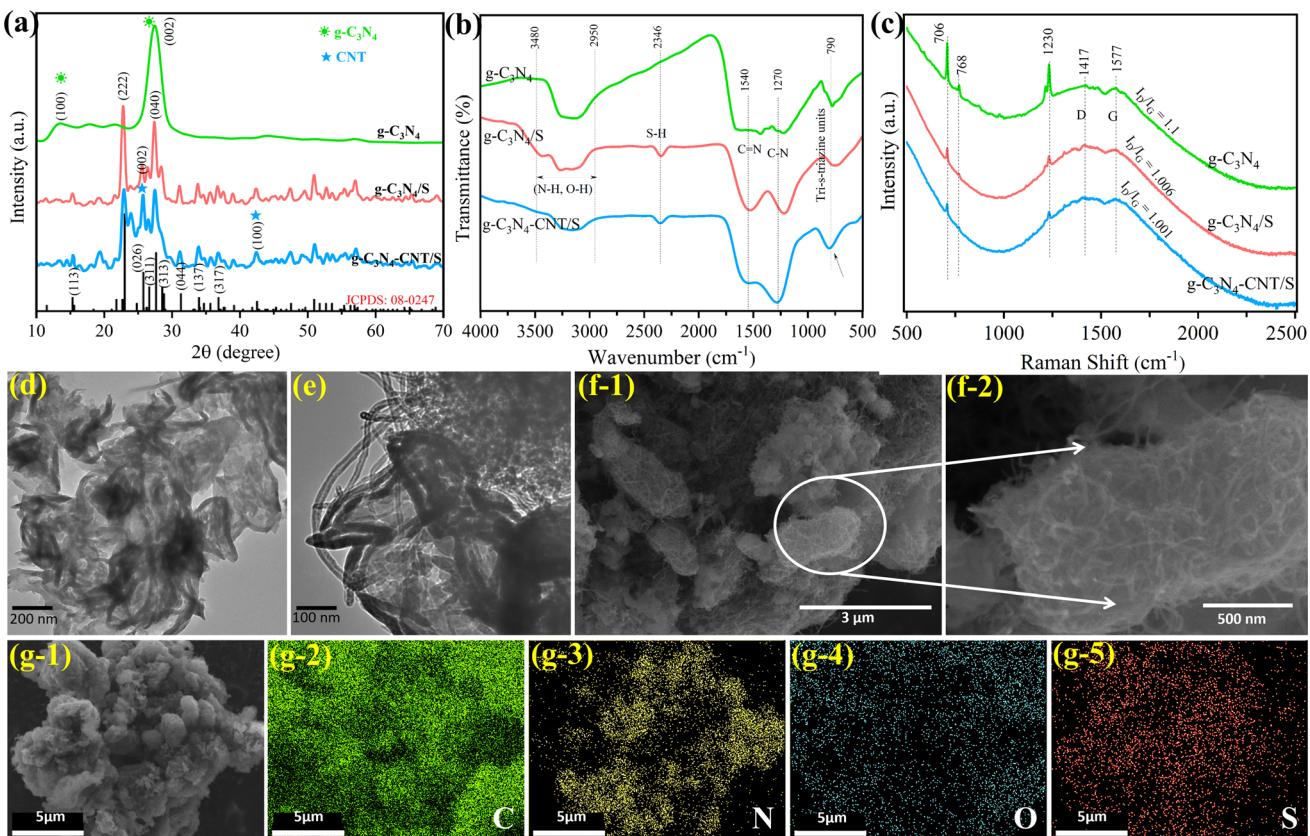
Fig. 1 For g-C_3N_4, g-C_3N_4/S, and g-C_3N_4-CNT/S: (a) XRD patterns, (b) FTIR spectra and (c) Raman spectra; TEM images for (d) g-C_3N_4 and (e) g-C_3N_4-CNT/S materials; (f) SEM images for g-C_3N_4-CNT/S; (g) color mapping of g-C_3N_4-CNT/S demonstrating the uniform distribution of C, N, O, and S elements.

crystalline nature of sulfur in the g-C_3N_4 or g-C_3N_4-CNT host. FTIR spectra in Fig. 1b reveal the characteristic features of g-C_3N_4, g-C_3N_4/S, and g-C_3N_4-CNT/S. The absorption band at 790 cm^{-1} signifies the out-of-plane skeletal bending modes of tri-s-triazine cycles, confirming the presence of g-C_3N_4.[40,41] Bands at 1270 and 1540 cm^{-1} correspond to the C–N stretching and CN heterocycle stretching modes of g-C_3N_4, respectively.[42] The broad band between 2950 and 3480 cm^{-1} indicates the stretching modes of terminal –NH groups at defect sites of the aromatic ring, and signals from S–H stretching modes (2347 cm^{-1}) align with reported observations.[43] The Raman spectra in Fig. 1c were recorded for g-C_3N_4, g-C_3N_4/S, and g-C_3N_4-CNT/S to assess the degrees of graphitization. Peaks around 706, 768, and 1230 cm^{-1} correspond to the breathing modes of the s-triazine ring in g-C_3N_4.[44] Distinct Raman peaks at 1417 and 1577 cm^{-1} represent the D band and G band, indicative of defects in disordered carbon and the in-plane vibration of graphitic layers, respectively.[45] The I_D/I_G intensity ratios decrease slightly with the addition of sulfur, which may be ascribed to the reduced disorder because of S particle encapsulation into void interlayers and defective sites of g-C_3N_4.[46] The results further signify a higher degree of the crystalline graphitic structure with improved electronic conduction, aligning with the XRD pattern in Fig. 1a. The porosity of g-C_3N_4, g-C_3N_4/S, and g-C_3N_4-CNT/S was studied through N_2 sorption

curves (Fig. S1†), indicating a type-IV nitrogen adsorption–desorption process with an H3 type hysteresis loop, suggesting mesopores. The BET surface area decreases from 82 m^2 g^{-1} for pure g-C_3N_4 to 64 and 49 m^2 g^{-1} for g-C_3N_4/S and g-C_3N_4-CNT/S, respectively, indicating successful impregnation of CNT and sulfur in pure g-C_3N_4 pores. Given that sulfur and Li_2S_2/Li_2S are insulators, good conductivity is crucial for the sulfur matrix. The conductivity of g-C_3N_4-CNT/S, probed by the four-point probe method, ranges between 10^{-2} and 10^{-3} S cm^{-1}, significantly higher than that of g-C_3N_4 materials, which falls between 10^{-12} and 10^{-13} S cm^{-1}.

The morphologies of the prepared active materials were investigated *via* TEM and SEM, complemented by elemental mapping. The TEM image in Fig. 1d displays g-C_3N_4 with loose morphology, featuring 2D nanosheets resulting from gas release during thermal polymerization. In contrast, the TEM image of g-C_3N_4-CNT/S (Fig. 1e) reveals 1D CNTs on 2D g-C_3N_4 sheets, with a clustered surface exhibiting wrinkles, curls, and sparse sulfur agglomerations. Abundant porosity benefits sulfur encapsulation, effectively accommodating volume variations during cycling. SEM images in Fig. 1f depict a well-maintained interlaced CNT network structure without noticeable sulfur agglomeration after sulfur diffusion into g-C_3N_4-CNT, indicating good sulfur dispersion in g-C_3N_4-CNT/S. Elemental mapping in Fig. 1g vividly illustrates uniform C, N, and S

15818 | *J. Mater. Chem. A*, 2024, **12**, 15814–15828

This journal is © The Royal Society of Chemistry 2024

dispersion throughout g-C$_3$N$_4$-CNT/S, with mappings completely following the shapes of the samples confirming uniform sulfur deposition on g-C$_3$N$_4$-CNT surfaces. From these results, we conclude that *in situ* growth of 1D CNTs on 2D g-C$_3$N$_4$ sheets constructs a cross-linked 3D conductive network, chemically bonded in the g-C$_3$N$_4$-CNT composite. This hybrid system provides an efficient electron transport path *via* CNTs, acting as a loading platform with N-containing functional groups to trap sulfur particles. The highly integrated g-C$_3$N$_4$-CNT/S with N-containing functional groups exhibits strong LiPS confinement, ensuring excellent cycling performance. Sulfur loading, a crucial LiSB performance index,[47] was calculated through the TGA of the g-C$_3$N$_4$-CNT/S composite. In Fig. S2,† the significant weight loss between 200 and 340 °C corresponds to sulfur evaporation, yielding a 68.6% sulfur content in g-C$_3$N$_4$-CNT/S, consistent with the experimentally added 70% sulfur.

XPS was utilized to delve deeper into the chemical bonding of the g-C$_3$N$_4$-CNT/S composite. In Fig. 2, XPS survey spectra exhibit peaks at approximately 161.9, 226.4, 283.6, 397.7 eV, and 532.1 eV, assigned to S 2p, S 2s, C 1s, N 1s, and O 1s binding energies, respectively. The fitted curve of C 1s spectra of the hybrid g-C$_3$N$_4$-CNT composite presents five peaks: –C–C– at 282.6 eV, conjugated –C=N–/–C=C– at 284.6 eV, S–C/C–N at 285.5 eV, and –S–C=N at 288.4 eV.[48] The red shifting of –C–C– from the usual 284 ± 0.5 eV could be due to the increase in electronic density around carbon, which causes the binding energy of –C–C– to shift to lower values. The computational

simulations by Priyanga *et al.*[49] suggest that the valence band (VB) originates from the P$_z$ orbitals of nitrogen atoms, while the conduction band (CB) arises from the P$_z$ orbitals of carbon atoms.[49] Consequently, the process of reduction and oxidation occurs at carbon and nitrogen atoms, respectively. This phenomenon stems from nitrogen's higher electronegative potential compared to carbon.[50] A 286.8 eV binding energy of g-C$_3$N$_4$-CNT is related to the C=O groups and originates from the CNTs after thermal annealing.[51] The N 1s spectra reveal four peaks at 397.5 eV, 398.5, 400.7, and 404.4 eV, attributed to pyridinic-like N in CN, –S–N=C–, graphitic-like N (C$_3$–N)/amino N (N–H), and oxidized N (N–O), respectively.[52] Abundant pyridinic N content in g-C$_3$N$_4$-CNT/S enhances lithium polysulfide adsorption *via* Li–N interaction, thereby reducing the barrier height and improving conductivity and electron density.[53,54] The S 2p spectrum of g-C$_3$N$_4$-CNT/S displays peaks at 162.5 (S 2p$_{3/2}$) and 163.9 eV (S 2p$_{1/2}$), assigned to –S–S– bonds (S$_8$ molecules).[55] Interestingly, the red shift in both the peaks (compared to XPS of pure S$_8$: S 2p$_{3/2}$ at 164 eV and S 2p$_{1/2}$ at 165 eV)[56] indicates a covalent link of sulfur chains to the host material.[57] The S 2p peak at 167.02 eV is ascribed to sulfate species, formed through chemical interaction between surface oxygen-containing functional groups and sulfur atoms.[58,59] Besides N, C, and S, oxygen (O) is detected, originating from oxygenated functional groups in g-C$_3$N$_4$ preparation at high temperatures. These oxygenated groups aid in chemically adsorbing sulfur and preventing polysulfides from dissolving into electrolytes effectively.[60,61]
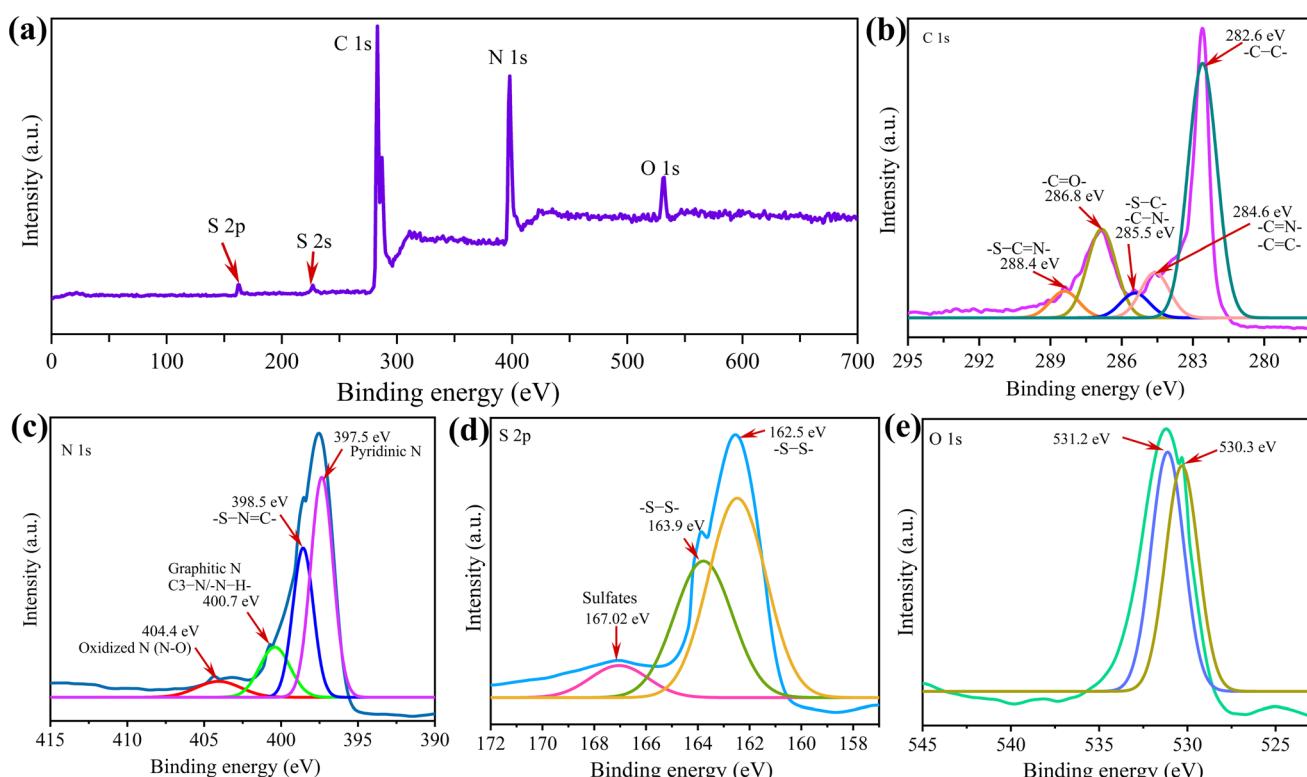
Fig. 2 (a) XPS spectrum showing the complete scan and the corresponding spectra for the elements (b–e) present in the g-C$_3$N$_4$-CNT/S composite.

This journal is © The Royal Society of Chemistry 2024

J. Mater. Chem. A, 2024, **12**, 15814–15828 | **15819**

The catalytic conversion process of LiPSs involves two steps: adsorption and catalytic reaction.[58,62] To assess adsorption ability, g-C$_3$N$_4$, and g-C$_3$N$_4$-CNT materials were individually immersed in a Li$_2$S$_6$ solution with magnetic stirring for 30 minutes. After 24 hours, adsorbents were retrieved, and optical photos of solutions were captured (inset of Fig. 3). Notably, the original light-yellow color of the Li$_2$S$_6$ solution becomes colorless after immersing in g-C$_3$N$_4$-CNT, suggesting effective absorption of most polysulfides. In contrast, the Li$_2$S$_6$ solution color shows a slight change after immersing in g-C$_3$N$_4$. Moreover, UV-vis measurements for Li$_2$S$_6$ reveal a strong absorption band in the 240–300 nm region, assigned to S$_6^{2-}$ polysulfide species.[63] g-C$_3$N$_4$ exhibits lower absorbance than the Li$_2$S$_6$ sample, while g-C$_3$N$_4$-CNT demonstrates the lowest absorbance, attributed to its high pyridinic/pyrrolic N content. This confirms the strong affinity between polysulfides and pyridinic/pyrrolic N, particularly effective in suppressing polysulfide dissolution in the electrolyte (S$_x$–Li···N interactions).[64] This robust affinity contributes significantly to enhancing the cycling stability of the sulfur electrode.

Theoretical calculations

We performed DFT calculations to assess and compare the binding strengths of S$_8$/LiPSs on g-C$_3$N$_4$ and g-C$_3$N$_4$-CNT composite surfaces. The calculated binding energies (E_b in eV) of S$_8$/LiPSs on the g-C$_3$N$_4$ surface align with prior study findings.[65] Tables S1–S3† and Fig. 4 offer a comprehensive analysis of the electronic and binding properties of both g-C$_3$N$_4$ and g-C$_3$N$_4$-CNT composite surfaces when interacting with S$_8$/LiPSs. The GGA-PBE bandgap for g-C$_3$N$_4$ and g-C$_3$N$_4$-CNT was determined to be approximately 1.195 and 0.049 eV, respectively (Table S1†). Regarding bandgap changes, notable decreases were observed, as seen in Li$_2$S (1.7321 to 0.0152 eV) and Li$_2$S$_2$ (0.0383 to 0.0354 eV), indicating a potential enhancement in g-C$_3$N$_4$-CNT electronic conductivity. Conversely, an increase in the bandgap for Li$_2$S and S$_8$ when interacting with g-C$_3$N$_4$ implies a reduction in electronic conductivity, as a larger bandgap typically requires more energy for electron movement

Fig. 3 UV-vis spectra for blank Li$_2$S$_6$ and Li$_2$S$_6$ added with CN and g-C$_3$N$_4$-CNT. The inset shows the digital picture of the effect of the active material on the adsorption of LiPSs in Li$_2$S$_6$ solution.

between the valence and conduction bands, hindering electronic transport. Binding energy changes, representing the strength of interactions, show varying values across the systems, with Li$_2$S displaying a substantial binding energy decrease (8.309 to 1.618 eV). These findings suggest that the adsorption of S$_8$/LiPSs onto g-C$_3$N$_4$ and g-C$_3$N$_4$-CNT composite surfaces leads to modifications in electronic and binding properties, with potential implications for the overall performance of the material. These outcomes suggest that the adsorption of S$_8$/LiPSs onto g-C$_3$N$_4$-CNT results in favorable alterations in electronic and binding properties, potentially enhancing the material's overall performance. Notably, for all lithium contents (Li$_2$S$_n$, $n = 1, 2, 4, 6, 8$), the LiPS molecules exhibit higher binding energies on the g-C$_3$N$_4$ surface compared to the g-C$_3$N$_4$-CNT surface (Fig. 4a–c). This observation suggests a more robust interaction between LiPSs and the g-C$_3$N$_4$ surface than with the g-C$_3$N$_4$-CNT surface. The structural impact becomes evident as the g-C$_3$N$_4$ layer undergoes distortion upon the adsorption of S$_8$/LiPS molecules (Fig. 4a), while the geometry of the CNT (S$_8$/LiPSs + g-C$_3$N$_4$-CNT) remains nearly unaltered (Fig. 4b). However, due to the weak van der Waals interaction between S$_8$/LiPSs and g-C$_3$N$_4$-CNT, a small strain can be observed on the g-C$_3$N$_4$ surface as well. This discrepancy indicates that LiPSs are chemically and physically adsorbed on g-C$_3$N$_4$ and g-C$_3$N$_4$-CNT, respectively, providing a rationale for the experimental phenomena discussed in Fig. 3. A thorough discussion on binding energy is included in the ESI.†

Upon closer examination of the structures, it is observed that all carbon (C) atoms and a quarter of the nitrogen (N) atoms in g-C$_3$N$_4$ are three-fold coordinated, with the remaining three-quarters of N atoms being two-fold coordinated. Analyzing the optimized structure of LiPS molecules on the g-C$_3$N$_4$ surface reveals that the interactions predominantly stem from chemical bonds between Li$^+$ atoms and the two-fold coordinated N atoms (Fig. 4a). This underscores that the atomic under-coordination in g-C$_3$N$_4$ plays a pivotal role in stabilizing LiPSs. In the case of Li$_2$S$_2$ and Li$_2$S, Li$^+$ forms bonds with N atoms, and S^{2-} binds with C on the polar g-C$_3$N$_4$ surface. Importantly, this explains the absence of chemical bonds between LiPSs and g-C$_3$N$_4$-CNT (Fig. 4b), where all C atoms are three-fold coordinated within the carbon nanotube. In-depth insights into the electrochemical reaction kinetics enhancement on both g-C$_3$N$_4$ and g-C$_3$N$_4$-CNT surfaces are sought by examining the complete reaction pathway involving the transformation of S$_8$ to Li$_2$S. In Fig. 4d, we show the landscape of relative Gibbs free energy (in eV) for the discharging process from S$_8$ (solid) to Li$_2$S (liquid) on both the g-C$_3$N$_4$ and the g-C$_3$N$_4$-CNT composite surfaces. It is noteworthy that the results of g-C$_3$N$_4$ differ significantly from those of g-C$_3$N$_4$-CNT. We hypothesize that in the case of g-C$_3$N$_4$, the transition from S$_8$ → Li$_2$S results in the generation of increasingly ionic structures where Li transforms into Li$^+$ and the energy becomes highly negative, indicating the discharged structure. On the other hand, for the g-C$_3$N$_4$-CNT composite surface, the interaction between LiPSs and CNT is limited, and we do not observe the same extent of electron transfer. The composite structure of g-C$_3$N$_4$-CNT may be oversimplified, as some of the LiPSs interact with the CNT, while other sulfides
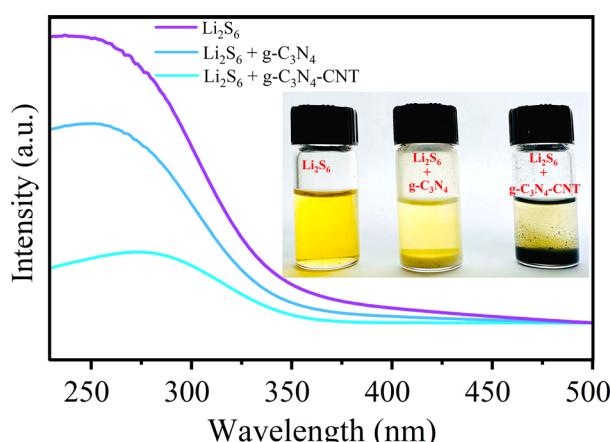
15820 | J. Mater. Chem. A, 2024, **12**, 15814–15828

This journal is © The Royal Society of Chemistry 2024
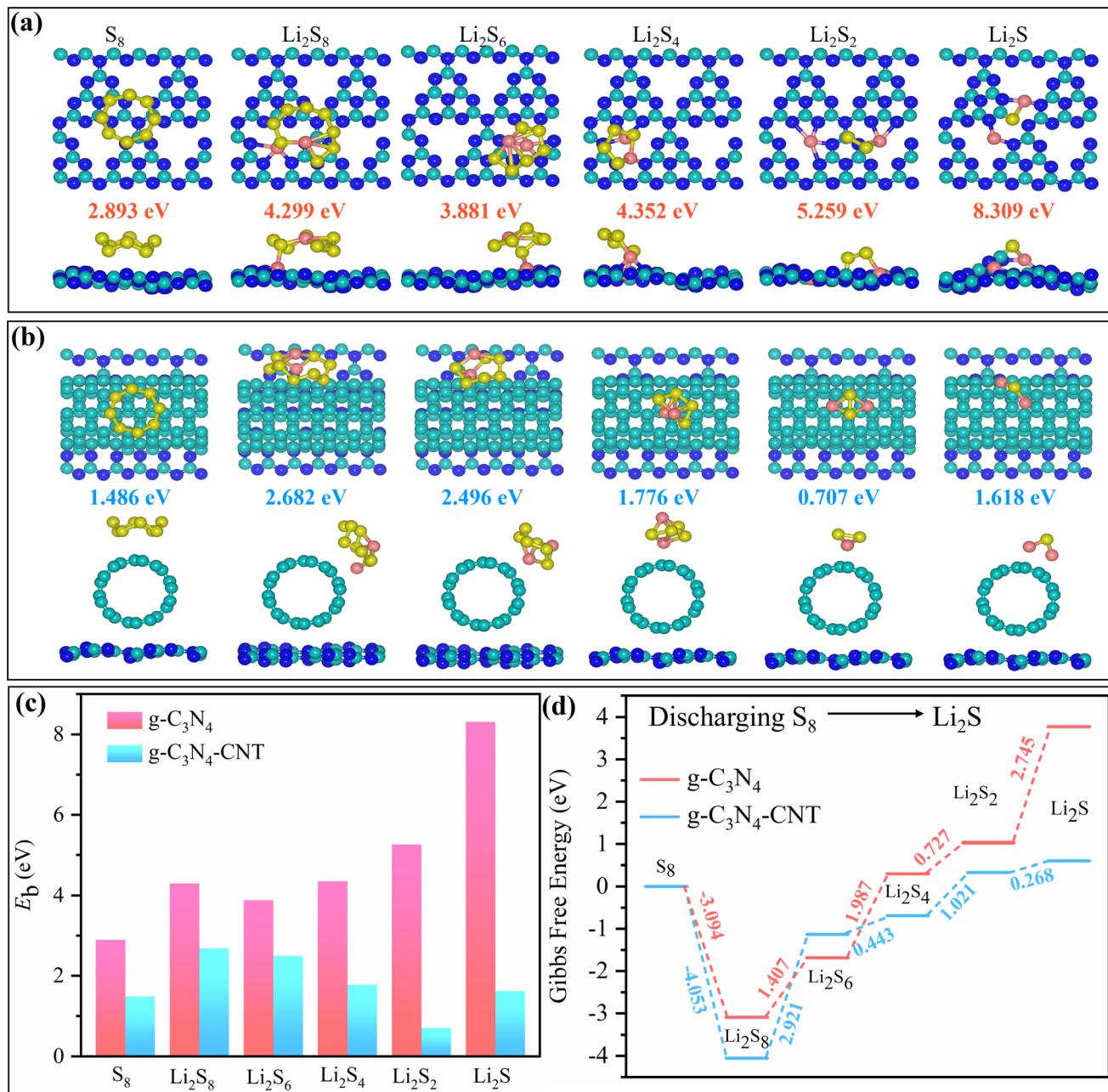
Fig. 4 Optimized configurations of LiPSs on the surfaces of (a) g-C$_3$N$_4$ and (b) the heterostructure of g-C$_3$N$_4$-CNT. The yellow, pink, cyan, and blue spheres represent sulfur (S), lithium (Li), carbon (C), and nitrogen (N) atoms, respectively. Panel (c) displays the binding energies and panel (d) illustrates the relative free energy for the discharging process from S$_8$ to Li$_2$S on both g-C$_3$N$_4$ and g-C$_3$N$_4$-CNT surfaces.

interact with g-C$_3$N$_4$, resulting in a mixture of outcomes. A thorough discussion on the Gibbs free energy uphill process is included in the ESI.†

The initial phase of the discharge process involves the simultaneous double reduction of an S$_8$ molecule and 2Li$^+$ ions, resulting in the formation of a lengthy Li$_2$S$_8$ polysulfide chain. Subsequently, Li$_2$S$_8$ undergoes further reduction, sequentially forming three intermediate LiPSs (Li$_2$S$_n$ = 6, 4, 2), ultimately leading to the production of the end-product Li$_2$S polysulfides. The obtained data unequivocally indicate a higher thermodynamic favorability of the discharging process on the g-C$_3$N$_4$-

CNT composite surface compared to the g-C$_3$N$_4$ surface, providing a rationale for the experimental phenomena discussed in Fig. 5. Specifically, the reaction energy from solid S$_8$ to liquid Li$_2$S$_8$ on the g-C$_3$N$_4$-CNT surface is more exothermic than that on the g-C$_3$N$_4$ surface (Fig. 4d). Notably, the subsequent four reduction stages from Li$_2$S$_8$ to Li$_2$S exhibit endothermic behavior on the g-C$_3$N$_4$ as well as on the g-C$_3$N$_4$-CNT composite surface. The final two steps, from Li$_2$S$_4$ to Li$_2$S$_2$ and from Li$_2$S$_2$ to Li$_2$S, exhibit substantial energy barriers (∼3.472 eV) compared to the other steps on both the g-C$_3$N$_4$ and g-C$_3$N$_4$-CNT composite substrates. This observation suggests that the

This journal is © The Royal Society of Chemistry 2024

J. Mater. Chem. A, 2024, **12**, 15814–15828 | **15821**
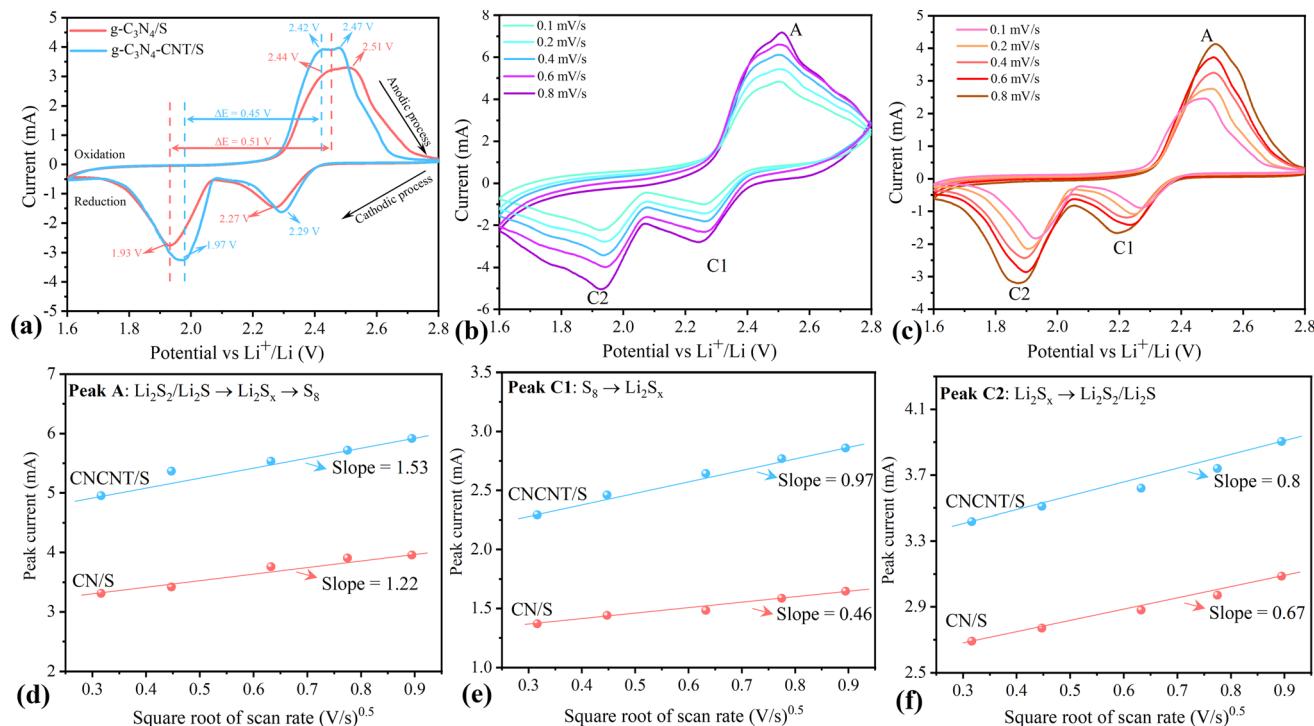
Fig. 5 (a) CV profiles for g-C$_3$N$_4$/S and g-C$_3$N$_4$-CNT/S cathodes; CV curves at different scan rates for (b) g-C$_3$N$_4$-CNT/S and (c) g-C$_3$N$_4$/S; plots of the peak currents *versus* the square root of scan rates from the CV curves of g-C$_3$N$_4$-CNT/S and g-C$_3$N$_4$/S cathodes for (d) Peak A, (e) Peak C1 and (f) Peak C2.

precipitation process of Li$_2$S$_2$/Li$_2$S is the rate-limiting step during discharging. In contrast, on the g-C$_3$N$_4$-CNT composite surface, the energy barrier for the endothermic precipitation process is effectively lowered (~1.289 eV), signifying a more favorable discharge. Additionally, the mixed behavior in the subsequent reductions correlates with the bandgap values, suggesting that electronic properties play a crucial role in the energetics of the discharge process. The lower bandgap of g-C$_3$N$_4$-CNT may contribute to its overall more favorable Gibbs free energy values, suggesting better electrochemical performance compared to the g-C$_3$N$_4$ substrate. These findings contribute crucial insights into the kinetics of the discharge process on both g-C$_3$N$_4$ and g-C$_3$N$_4$-CNT substrates, highlighting key rate-determining steps and their corresponding energy landscapes. Furthermore, the electronically conductive nature of the g-C$_3$N$_4$-CNT surface facilitates rapid electron transfer between C atoms (from CNT) of g-C$_3$N$_4$-CNT and S atoms of LiPSs, thereby weakening the Li–S bonds of LiPSs. As a result, g-C$_3$N$_4$-CNT significantly reduces the reduction barrier of LiPSs, promotes Li$_2$S precipitation, and enhances reaction reversibility, underscoring its potential superiority over g-C$_3$N$_4$ in terms of electrochemical performance.

Electrochemical characterization

The electrochemical performance of g-C$_3$N$_4$/S and g-C$_3$N$_4$-CNT/S was assessed in a pouch cell configuration. In Fig. 5a, the CV curves of g-C$_3$N$_4$/S and g-C$_3$N$_4$-CNT/S composites are presented within a voltage range of 1.6 V to 2.8 V at a sweep rate of 0.05 mV s^{-1}. During the cathodic scan, both g-C$_3$N$_4$/S and g-C$_3$N$_4$-CNT/S

exhibit two main reduction peaks. The peak at approximately 2.27 V corresponds to the reduction of elemental sulfur to high-order polysulfides, Li$_2$S$_n$ ($4 \leq n \leq 8$), while the peak between 1.9 and 2.0 V signifies the formation of Li$_2$S$_2$/Li$_2$S from low-order polysulfides.[66] In the anodic scanning process, two oxidation peaks between 2.44 and 2.51 V are associated with the oxidation of Li$_2$S$_2$/Li$_2$S to long-chain polysulfides (Li$_2$S$_n$ ($n > 2$)) and further to sulfur.[67] Compared to g-C$_3$N$_4$/S, the main cathodic peaks of g-C$_3$N$_4$-CNT/S exhibit a slight shift to higher reduction potential, and the anodic peaks shift to lower oxidation potential, indicating reduced polarization in g-C$_3$N$_4$-CNT/S. This facilitates polysulfide conversion, indicating improved reversibility of the electrode during cycling.[68] Furthermore, the smaller potential difference (ΔE) between cathodic and anodic peak current densities in g-C$_3$N$_4$-CNT/S reflects its remarkably stable tendency to effectively suppress the diffusion of liquid intermediate products during CV cycles.[69] Additionally, during the scanning process for g-C$_3$N$_4$-CNT/S (Fig. S3†), the cathodic peak position, peak current, and peak area exhibit minimal change over the next 5 cycles, indicating superior capacity retention and good reversibility of the cell. CV curves at various current rates are depicted in Fig. 5b and c for g-C$_3$N$_4$-CNT/S and g-C$_3$N$_4$/S cathodes, respectively. The cathodic processes involve Peak C1 and Peak C2, attributed to S$_8$ transformation to long-chain LiPSs (Li$_2$S$_n$, $4 \leq n \leq 8$) and the subsequent reduction of long-chain LiPSs to Li$_2$S$_2$/Li$_2$S, respectively.[66,70]

The anodic process is represented by Peak A, corresponding to the reverse transformation. The redox peaks at higher current rates appear broadened for both materials, indicating slow

15822 | *J. Mater. Chem. A*, 2024, 12, 15814–15828

This journal is © The Royal Society of Chemistry 2024

kinetics of LiPS conversion. Moreover, at increased scan rates, redundant peaks emerge after 2.6 V during the anodic scan for both materials, signifying sluggish cathode kinetics. Overall, g-C$_3$N$_4$-CNT/S exhibits higher peak current densities than g-C$_3$N$_4$/S, indicating enhanced Li$^+$ transportability and superior rate capability. Additionally, both cathodic and anodic peak currents for both materials exhibit a linear relationship with the square root of the scan rate ($v^{0.5}$), suggesting diffusion-limited discharge/charge reactions (Fig. 5d–f).

Therefore, the diffusion coefficient of Li$^+$ can be described by the Randles–Sevcik equation:[71] $I_P = (2.69 \times 10^5)n^{1.5}AD^{0.5}C_{Li^+}^{0.5}v^{0.5}$, in which n is the number of charge transfers, A is the active electrode area, D is the Li$^+$ diffusion coefficient, and C_{Li^+} is the concentration of Li$^+$ in bulk. Since n, A, and c_0 are constants, $\frac{I_P}{v^{0.5}} \propto D^{0.5}$, a larger $\frac{I_P}{v^{0.5}}$ implies a higher D. The equation reveals a linear relationship between the peak current and the square

root of the scan rate, with the slope indicating lithium-ion diffusion.[72] Notably, in g-C$_3$N$_4$-CNT/S, the slopes for the two reduction peaks and one oxidation peak surpass those in g-C$_3$N$_4$/S at the same electrode area for each sulfur reduction and oxidation reaction. This suggests accelerated Li ion diffusivity and improved LiPS redox kinetics during discharge/charge processes attributed to CNT presence, promoting LiPS transformation and facilitating rapid Li$^+$ migration.[73] However, due to the formation of various polysulfides in the redox process, quantifying D_{Li^+} is challenging due to an unknown number of electrons involved in polysulfide formation.

Galvanostatic charge–discharge tests were conducted to investigate the electrochemical performance of the pouch cells. In Fig. 6a, the 1st cycle charge–discharge voltage profiles of g-C$_3$N$_4$/S and g-C$_3$N$_4$-CNT/S cathodes at a 0.1C current density reveal two distinct discharging voltage plateaus and one major charging voltage plateau, consistent with the multistep
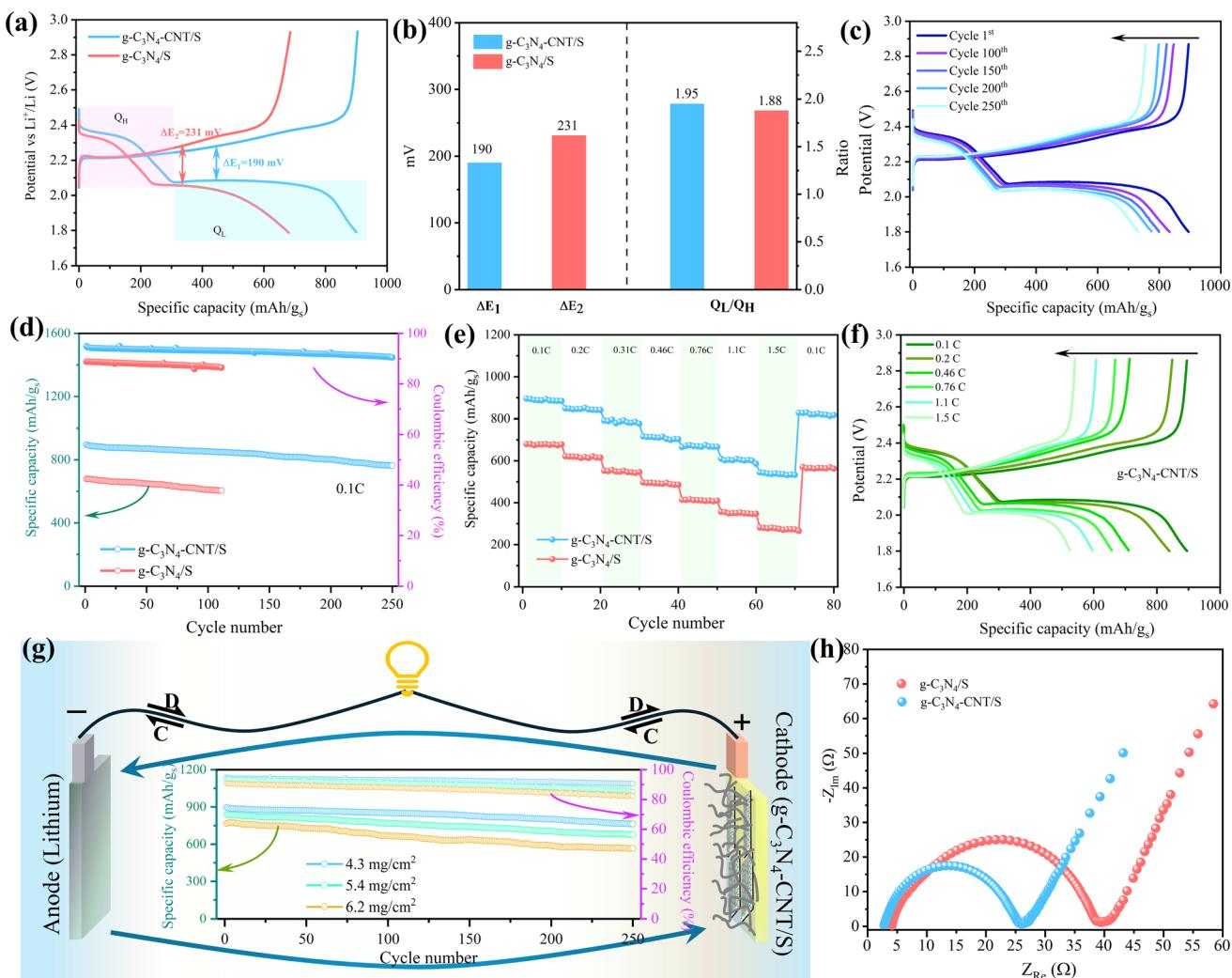
Fig. 6 (a) Initial charge–discharge curves for the g-C$_3$N$_4$/S and g-C$_3$N$_4$-CNT/S cathodes at 0.1C, (b) the capacity contribution of Q_H, Q_L, and the Q_L/Q_H ratio of g-C$_3$N$_4$-CNT/S and g-C$_3$N$_4$/S at 0.1C, (c) galvanostatic charge–discharge profiles of the g-C$_3$N$_4$-CNT/S cathode for 250 cycles, (d) cycle performance and coulombic efficiency of g-C$_3$N$_4$/S and g-C$_3$N$_4$-CNT/S cathodes for 110 and 250 cycles, respectively, (e) rate capabilities of g-C$_3$N$_4$/S and g-C$_3$N$_4$-CNT/S cathodes under various current densities, (f) galvanostatic charge–discharge profiles of the g-C$_3$N$_4$-CNT/S cathode at different current densities, (g) cycle performance of the g-C$_3$N$_4$-CNT/S cathode with varied sulfur loading for 250 cycles at 0.1C and (h) EIS spectra of the freshly prepared uncycled cell.

This journal is © The Royal Society of Chemistry 2024

J. Mater. Chem. A, 2024, **12**, 15814–15828 | **15823**

reduction of sulfur indicated by CV curves. The polarization potential (ΔE), calculated as the gap between anode and cathode peaks, is lower for g-C_3N_4-CNT/S (190 mV) compared to g-C_3N_4/S (231 mV), reflecting reduced polarization in the g-C_3N_4-CNT/S electrode facilitated by CNT-N active site catalysis. Additionally, the capacity of the lower discharge plateau (Q_L) and higher discharge plateau (Q_H) is calculated from discharge curves. The higher Q_L/Q_H signifies superior electrocatalytic activity for polysulfides, where Q_H corresponds to sulfur conversion into soluble polysulfides, and Q_L represents efficient reduction of polysulfides to Li_2S.[74] In Fig. 6b, the capacity ratio for g-C_3N_4-CNT/S (1.95) surpasses that of CN/S (1.88), indicating enhanced sulfur utilization owing to the superior catalytic activity of S_x–Li···N in the g-C_3N_4-CNT/S electrode. The charge–discharge profiles of g-C_3N_4-CNT/S at 0.1C over 250 cycles (Fig. 6c) reveal sustained maintenance of the two discharge plateaus, demonstrating rapid mass transport and reaction kinetics. A comparison of long-term cycle performances between g-C_3N_4/S and g-C_3N_4-CNT/S (Fig. 6d) illustrates the initial capacity decay attributed to the activation process. Non-activated sulfur may aggregate on g-C_3N_4's surface initially leading to the formation of an unstable solid electrolyte interface (SEI) layer.[75] The subsequent cycles witness enhanced sulfur utilization and uniform depreciation in capacity, with g-C_3N_4-CNT/S delivering an initial discharge capacity of 895.7 mA h g^{-1} and a capacity retention of 86% after 250 cycles, boasting a CE of 90.4%. In contrast, g-C_3N_4/S achieves a reversible initial discharge capacity of 679.6 mA h g^{-1}. The improved cycle performance of g-C_3N_4-CNT/S is attributed to abundant anchor sites on nanosheets, influencing LiPS adsorption. Rate performance (Fig. 6e) indicates higher discharge capacity of g-C_3N_4-CNT/S than g-C_3N_4/S at different current rates, with g-C_3N_4-CNT/S recovering well at 0.1C, which is ascribed to the porous structures of g-C_3N_4 ensuring fast Li ion transportation and chemical confinement for lithium polysulfides.[27,76] Charge–discharge curves at various rates (0.1C to 1.5C) for g-C_3N_4-CNT/S (Fig. 6f) demonstrate excellent maintenance of discharge plateaus at 1.5C, affirming swift mass transport and reaction kinetics. The cathode exhibits high reversibility, maintaining capacities of 847, 656, and 543 mA h g^{-1} at 0.2, 0.76, and 1.5C, respectively, corresponding to 95%, 73%, and 61% of the original capacity. High sulfur mass loading is crucial for achieving elevated energy density and facilitating lithium–sulfur battery commercialization. Therefore, pouch cells, featuring sulfur loadings of 4.3, 5.4, and 6.2 mg cm^{-2}, underwent testing at 0.1C for the g-C_3N_4-CNT/S cathode. In Fig. 6g, the 6.2 mg cm^{-2} cell yields the lowest reversible discharge capacity of 566 mA h g^{-1} after 250 cycles, exhibiting a fading rate of 0.08% per cycle and a CE of 82%. This underscores g-C_3N_4-CNT/S's outstanding electrochemical performance under high-loading configurations, indicating robust LiPS inhibition and accelerated kinetic conversion for enhanced sulfur utilization.[77] Table S4† provides a comparative overview of Li–S batteries, affirming the remarkable performance of the g-C_3N_4-CNT/S cathode in the pouch cell format (electrode size ∼22 cm^2 and E/S ∼5 μl mg^{-1}) as compared to the coin cells with a low electrode size (∼1.6 cm^2) and flooded electrolyte (E/S > 15 μl mg^{-1}). The large area

pouch cells are more prone to uneven sulfur degradation,[78] which would increase the electrode tortuosity and even block the electrolyte redistribution, thereby reducing the cycling performance and CE of the pouch cell.[79] Therefore, the superior performance of our composite electrode further attests to its utilization for commercial applications.

To further detail improved conductivity and enhanced polysulfide-trapping ability, EIS measurements for cells with g-C_3N_4/S and g-C_3N_4-CNT/S cathodes were conducted (Fig. 6h) in the frequency range of 0.5 Hz–2 mHz, with an excitation potential of 10 mV and 20 points per decade. Nyquist plots reveal three frequency regions: a high-frequency segment indicating electrolyte resistance (R_e), a middle-frequency semicircle corresponding to charge transfer impedance (R_{ct}), and a low-frequency spike representing Warburg impedance (W) associated with lithium-ion diffusion in the cathode.[80,81] As can be seen, the semicircle diameter and R_{ct} value for the g-C_3N_4-CNT/S cathode cell (22.6 Ω) are notably lower than those of the g-C3N4/S cathode cell (35.6 Ω), indicating reduced charge transfer resistance due to enhanced electrical conductivity and improved electrical contact upon CNT incorporation into g-C_3N_4. Additionally, the R_e for g-C_3N_4-CNT/S is merely 2.7 Ω, affirming outstanding cell conductivity. This outcome underscores lower electrochemical impedance in the g-C_3N_4-CNT/S host, attributed to the presence of CNTs and abundant pyridine N acting as chemically active sites that robustly adsorb polysulfides, facilitate charge and ion transfer, and diminish electrode–electrolyte interface resistance and charge transfer resistance. Parameters from the Nyquist plot are detailed in Table S5.† To showcase the superior mechanical flexibility of the designed g-C_3N_4-CNT/S electrodes, various folding angles for pouch cells were tested. Fig. 7 reveals impressive open circuit voltage (OCV) stability at 2.36 V, successfully powering an LED bulb at varying bending angles. Remarkably, no discernible change in LED brightness or OCV readings occurred even at nearly 180° bending angles. The g-C_3N_4-CNT/S-based Li–S pouch cells demonstrate favorable electrical performance, emphasizing their practical utility in flexible energy systems, owing to excellent cycling stability achieved through effective polysulfide shuttling suppression.

Postmortem analysis

The lithiation mechanism of the g-C_3N_4-CNT/S cathode was explored through XPS analysis after the 250th discharge cycle. The pouch cell was dismantled in an argon-filled glovebox, and a 10 mm × 10 mm segment of the g-C_3N_4-CNT/S cathode was cut and dried before XPS measurements. Fig. 8 exhibits well-defined peaks for C, N, S, and O, consistent with the pure active material, revealing some new bond formations. Notably, additional elements (Li and F) were observed. In the C 1s spectra, peaks at 282.6 eV, 284.4, 286.6, and 288.3 eV corresponded to –C–C–, –C=N–/–C=C–, C=O, and –S–C=N, mirroring the active material's C 1s spectra in Fig. 2. However, a new peak at 292.5 eV, representing C–F due to electrolyte passivation, emerged. Deconvoluting the N 1s spectra revealed peaks at 397.5 eV for pyridinic-like N (–C=N–) in the CNT
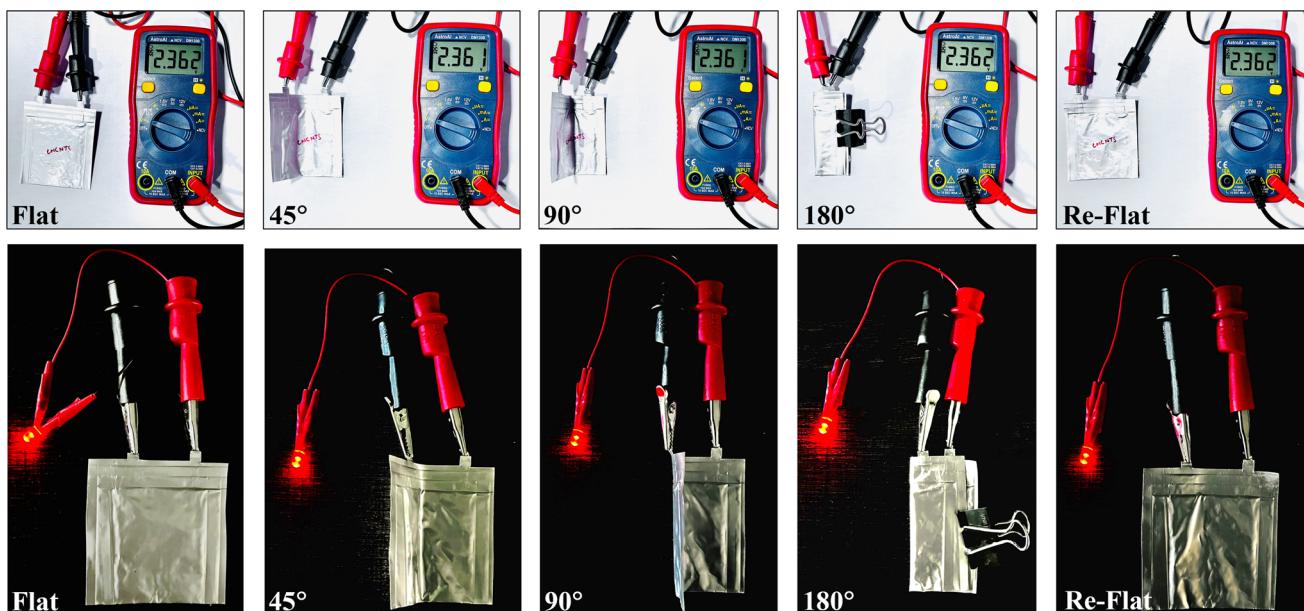
Fig. 7 Upper row: digital pictures of the OCV for the pouch cell consisting of the g-C$_3$N$_4$-CNT/S cathode at different folding angles and bottom row: pictures of LEDs lit up by the pouch cell at different folding angles demonstrating the excellent flexibility of the developed pouch cell.

structure, 399.1 eV for –S–N=C–, and 403.6 for oxidized N (N–O).[82] The 396.7 eV peak confirmed Li–N bond formation during cathode lithiation, contributing to lithium storage.[83] Additionally, the 407.2 eV peak indicated nitrate (NO$_3^-$) presence on the cathode, formed by LiNO$_3$ reduction during cycling and hindering active material reversibility.[84] For S 2p, various reduction products and intermediates were identified after

cycling including Li$_2$S$_2$–S at 164.5 eV, thiosulfates at 167.2 eV, sulfites at 168.0 eV, and S–F bonds at 169.1 eV.[85] Compared to the S-spectra in Fig. 2, more sulfates were observed in the cycled cathode, which could result from oxidized S-species from the reaction between LiPSs and oxygen species. The O–S bond emerged due to sulfate species interacting with residual oxygen-containing species, and the S–F bond indicated strong covalent
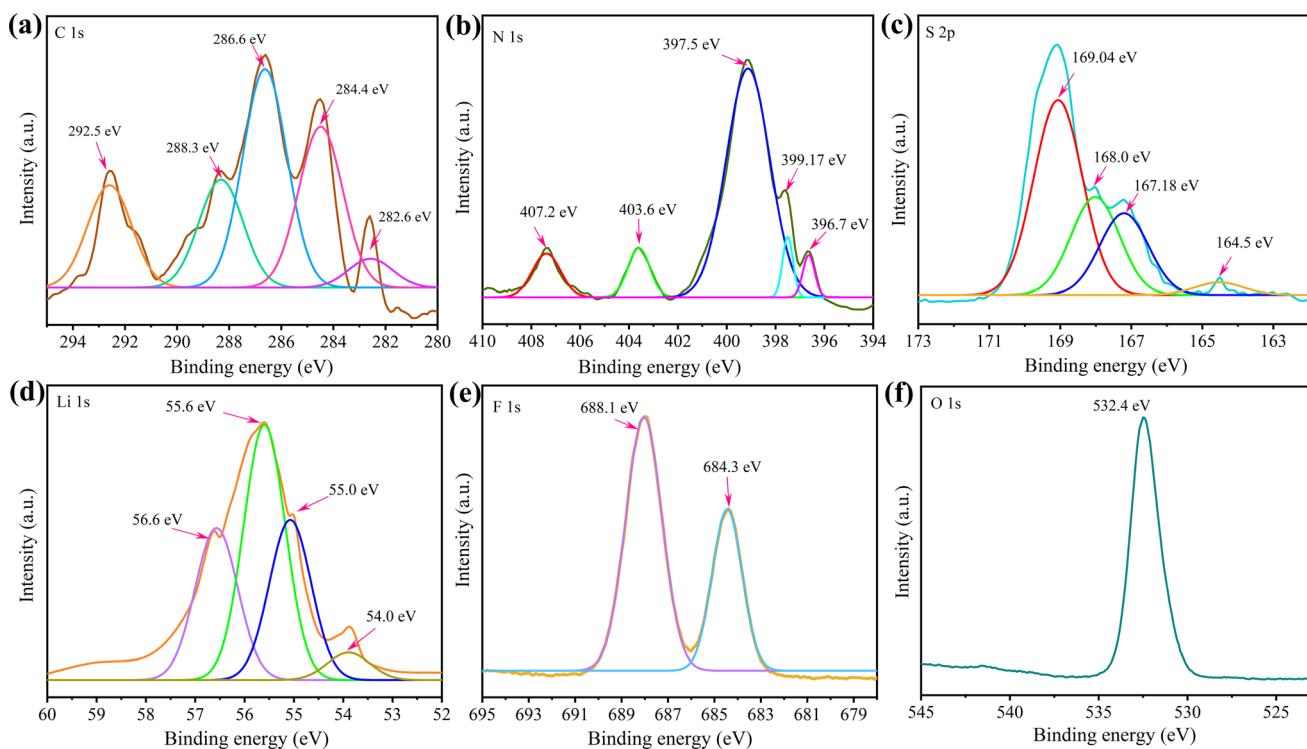

Fig. 8 (a–f) XPS spectra of the g-C$_3$N$_4$-CNT/S cathode obtained from the pouch cell cycled for 250 charge–discharge cycles.

This journal is © The Royal Society of Chemistry 2024

J. Mater. Chem. A, 2024, **12**, 15814–15828 | **15825**

interaction between F-containing electrolytes and poly-sulfides.[86] Interestingly, the doublet peaks at around 163 eV representing S $2p_{3/2}$ and S $2p_{1/2}$ for elemental sulfur were absent in the cycled cell. This agrees with the fact that a fully dis-charged cathode after 250 cycles should have all sulfur in the reduced state (Li_2S/Li_2S_2) and the absence of a doublet peak confirms that no 'dead' sulfur was present on the cathode even after 250 cycles.[87] F 1s peaks at 684.3 and 688.1 eV reflected electrolyte and PVDF passivation, suggesting g-C_3N_4-CNT/elec-trolyte interaction during cycling. In Li 1s spectra, peaks at 54.0, 55.0, 55.6, and 56.3 denoted Li–C, Li–S, Li–N, and Li–O bond formations, signifying C=N bond involvement in lithium storage in addition to Li–S bonds during discharge.[12,64,88] Over-all, the XPS analysis of the cycled cell affirmed polysulfide adsorption on the g-C_3N_4-CNT surface.

To delve into the electrochemical kinetics of the cathodes, Fig. S5† displays the EIS results from the pouch cell cycled for 250 cycles (g-C_3N_4-CNT/S) and 110 cycles (g-C_3N_4/S) at 0.1C. As can be seen, after cycling, the R_e of the cell with g-C_3N_4-CNT/S as the cathode increases from 2.7 to 5.2 Ω, notably lower than the cell with g-C_3N_4/S as the cathode (rising from 4.2 to 11.1 Ω), signifying restricted polysulfide diffusion from g-C_3N_4-CNT/S. Moreover, the reduced R_{ct} for both cells (Table S5†) post-cycling suggests enhanced electrolyte penetration into the composite, shortening charge and ion transport paths.[84,89] Another observed semicircle at low frequency for the g-C_3N_4/S cathode (the second semicircle) may indicate resistance from an insulating layer like Li_2S (denoted as R_g), which incompletely converts to sulfur during charging.[90] In contrast, the cell with g-C_3N_4-CNT/S as the cathode exhibits a single semicircle, signi-fying an efficient redox reaction. The impedance spectra affirm that the well-designed g-C_3N_4-CNT/S not only enhances sulfur cathode conductivity but also mitigates the shuttle effect by retaining more polysulfides within the cathode.

Conclusion

In summary, a hierarchical architecture, featuring 1D CNTs grown on 2D g-C_3N_4 sheets, is synthesized as a host matrix for a sulfur cathode in Li–S pouch cells. Experimental analyses reveal the g-C_3N_4-CNT/S composite's high pyridine N content, promoting robust interactions with LiPSs and inhibiting poly-sulfide shuttling, thereby enhancing electrochemical perfor-mance in Li–S batteries. DFT studies provide valuable insights through a comprehensive examination of the electronic bandgap, binding energy, and relative Gibbs free energy alter-ations upon the interaction of S_8/LiPSs with both g-C_3N_4 and g-C_3N_4-CNT composite surfaces. While g-C_3N_4 exhibits increased bandgap values for Li_2S and S_8, indicative of reduced electronic conductivity, g-C_3N_4-CNT demonstrates a decrease in the bandgap, suggesting improved electronic properties. Addition-ally, changes in binding energy highlight distinct interactions between g-C_3N_4 and g-C_3N_4-CNT with S_8/LiPSs. The relative Gibbs free energy landscape further highlights differences, with g-C_3N_4-CNT showcasing higher thermodynamic favorability in the discharging process compared to g-C_3N_4. These findings collectively contribute to a nuanced understanding of the material dynamics, emphasizing the potential benefits of g-C_3N_4-CNT in enhancing the electrochemical performance in S_8/LiPS systems. As a result, the g-C_3N_4-CNT/S electrode achieves a capacity of 895 mA h g^{-1} at 0.1C with excellent high-rate, long-term cycling stability (0.053% capacity decay per cycle over 250 cycles). The electrode also attains a high discharge capacity of 566 mA h g^{-1} under a high sulfur loading of 6.2 mg cm^{-2} after 250 cycles, exhibiting a fading rate of 0.08% per cycle and flexibility during repeated bending. Postmortem XPS and EIS analyses further substantiate the excellent performance of the Li–S pouch cell by elucidating new bond formation and changes in cell resistance, respectively. The postmortem investigations from XPS show that the binding energy peaks of elemental S_8 are missing from the cycled cell, which means that no dead sulfur on the cathode side was present even after the 250th cycle, thus revealing the excellent potential of the g-C_3N_4-CNT host matrix for the sulfur cathode. This work lays the founda-tion for the rational design of an ideal S host, enabling cathodes with multifunctional adsorption-catalytic sites for Li–S batteries with prolonged cycling life and high-rate capability.

Author contributions

VKT: methodology, investigation, data curation, validation, and writing – original draft. RLK: DFT calculation and analysis. OTD: formal analysis and conceptualization. RM: methodology, data curation, and visualization. GCS: project administration and supervision. MS: conceptualization, review & editing, supervision, and project administration.

Conflicts of interest

All the authors declare that they have no known competing financial interests or personal relationships that could have appeared to influence the work reported in this paper.

Acknowledgements

References

1 A. G. Olabi and M. A. Abdelkareem, *Renewable Sustainable Energy Rev.*, 2022, **158**, 112111.

2 R. Xu, L. Du, D. Adekoya, G. Zhang, S. Zhang, S. Sun, Y. Lei, R. Xu, Y. Lei, L. Du, G. Zhang, S. Sun, D. Adekoya and S. Zhang, *Adv. Energy Mater.*, 2021, **11**, 2001537.

3 M. Fichtner, K. Edström, E. Ayerbe, M. Berecibar, A. Bhowmik, I. E. Castelli, S. Clark, R. Dominko, M. Erakca, A. A. Franco, A. Grimaud, B. Horstmann,

A. Latz, H. Lorrmann, M. Meeus, R. Narayan, F. Pammer, J. Ruhland, H. Stein, T. Vegge and M. Weil, *Adv. Energy Mater.*, 2022, **12**, 2102904.

4 A. G. Olabi, Q. Abbas, P. A. Shinde and M. A. Abdelkareem, *Energy*, 2023, **266**, 126408.

5 C. P. Grey and D. S. Hall, *Nat. Commun.*, 2020, **11**, 1–4.

6 Y. Tian, G. Zeng, A. Rutt, T. Shi, H. Kim, J. Wang, J. Koettgen, Y. Sun, B. Ouyang, T. Chen, Z. Lun, Z. Rong, K. Persson and G. Ceder, *Chem. Rev.*, 2021, **121**, 1623–1669.

7 G. Zhou, H. Chen and Y. Cui, *Nat. Energy*, 2022, **7**, 312–319.

8 Y. Chen, T. Wang, H. Tian, D. Su, Q. Zhang and G. Wang, *Adv. Mater.*, 2021, **33**, 2003666.

9 Z. W. Seh, Y. Sun, Q. Zhang and Y. Cui, *Chem. Soc. Rev.*, 2016, **45**, 5605–5634.

10 Z. Han, S. Li, Y. Wu, C. Yu, S. Cheng and J. Xie, *J. Mater. Chem. A*, 2021, **9**, 24215–24240.

11 L. Huang, J. Li, B. Liu, Y. Li, S. Shen, S. Deng, C. Lu, W. Zhang, Y. Xia, G. Pan, X. Wang, Q. Xiong, X. Xia and J. Tu, *Adv. Funct. Mater.*, 2020, **30**, 1910375.

12 F. Zhao, J. Xue, W. Shao, H. Yu, W. Huang and J. Xiao, *J. Energy Chem.*, 2023, **80**, 625–657.

13 G. Gao, X. Yang, J. Bi, W. Guan, Z. Du and W. Ai, *J. Mater. Chem. A*, 2023, **11**, 26318–26339.

14 J. Wang and W. Q. Han, *Adv. Funct. Mater.*, 2022, **32**, 2107166.

15 D. Wang, J. Liu, X. Bao, C. Qing, T. Zhu and H. E. Wang, *ACS Appl. Energy Mater.*, 2022, **5**, 2573–2579.

16 Q. Zhao, X. Bao, L. Meng, S. Dong, Y. Zhang, C. Qing, T. Zhu and H. E. Wang, *J. Colloid Interface Sci.*, 2023, **644**, 546–555.

17 V. K. Tomer, O. A. T. Dias, A. Gouda, R. Malik and M. M. Sain, *Mater. Horiz.*, 2024, DOI: **10.1039/D4MH00200H**.

18 H. E. Wang, X. Li, N. Qin, X. Zhao, H. Cheng, G. Cao and W. Zhang, *J. Mater. Chem. A*, 2019, **7**, 12068–12074.

19 R. Zhe, T. Zhu, X. Wei, Y. Ren, C. Qing, N. Li and H. E. Wang, *J. Mater. Chem. A*, 2022, **10**, 24422–24433.

20 W. Sun, Z. Song, Z. Feng, Y. Huang, Z. J. Xu, Y. C. Lu and Q. Zou, *Nano-Micro Lett.*, 2022, **14**, 1–23.

21 S. A. Thomas, M. R. Pallavolu, M. E. Khan and J. Cherusseri, *J. Energy Storage*, 2023, **68**, 107673.

22 Y. Wang, L. Liu, T. Ma, Y. Zhang and H. Huang, *Adv. Funct. Mater.*, 2021, **31**, 2102540.

23 W. Sun, L. Xu, Z. Song, H. Lin, Z. Jin, W. Wang, A. Wang and Y. Huang, *Adv. Funct. Mater.*, 2023, 2313112.

24 Y. Li, Y. Deng, J. L. Yang, W. Tang, B. Ge and R. Liu, *Adv. Funct. Mater.*, 2023, **33**, 2302267.

25 H. Zou, Y. Zou, Y. Lv, Z. Ao, N. Chen and Y. Huang, *ACS Appl. Energy Mater.*, 2022, **5**, 10067–10075.

26 J. Wang, Z. Meng, W. Yang, X. Yan, R. Guo and W. Q. Han, *ACS Appl. Mater. Interfaces*, 2019, **11**, 819–827.

27 J. Zhang, J. Y. Li, W. P. Wang, X. H. Zhang, X. H. Tan, W. G. Chu and Y. G. Guo, *Adv. Energy Mater.*, 2018, **8**, 1702839.

28 G. Kresse and J. Furthmüller, *Phys. Rev. B: Condens. Matter Mater. Phys.*, 1996, **54**, 11169.

29 G. Kresse and J. Furthmüller, *Comput. Mater. Sci.*, 1996, **6**, 15–50.

30 G. Kresse and D. Joubert, *Phys. Rev. B: Condens. Matter Mater. Phys.*, 1999, **59**, 1758.

31 J. P. Perdew, K. Burke and M. Ernzerhof, *Phys. Rev. Lett.*, 1996, **77**, 3865.

32 S. Grimme, J. Antony, S. Ehrlich and H. Krieg, *J. Chem. Phys.*, 2010, **132**(15), 154104.

33 H. J. Monkhorst and J. D. Pack, *Phys. Rev. B: Solid State*, 1976, **13**, 5188.

34 V. Wang, N. Xu, J. C. Liu, G. Tang and W. T. Geng, *Comput. Phys. Commun.*, 2021, **267**, 108033.

35 D. Nepak, V. K. Tomer and K. Kailasam, in *Metal-free Functionalized Carbons in Catalysis*, ed. A. Villa and N. Dimitratos, Royal Society of Chemistry, UK, 2018, pp. 67–102.

36 R. Malik, N. Joshi and V. K. Tomer, *Coord. Chem. Rev.*, 2022, **466**, 214611.

37 R. Malik, V. K. Tomer, T. Dankwort, Y. K. Mishra and L. Kienle, *J. Mater. Chem. A*, 2018, **6**, 10718–10730.

38 V. K. Tomer, R. Malik and V. Chaudhary, *Appl. Mater. Today*, 2019, **16**, 193–203.

39 L. P. Yu, L. Xu, C. Shearer, X. H. Zhou and L. Lu, *Adv. Sustainable Syst.*, 2023, **7**, 2300061.

40 R. Malik, V. K. Tomer, N. Joshi, T. Dankwort, L. Lin and L. Kienle, *ACS Appl. Mater. Interfaces*, 2018, **10**, 34087–34097.

41 R. Malik, V. K. Tomer, V. Chaudhary, M. S. Dahiya, A. Sharma, S. P. Nehra, S. Duhan and K. Kailasam, *J. Mater. Chem. A*, 2017, **5**, 14134–14143.

42 R. Malik and V. K. Tomer, *Renewable Sustainable Energy Rev.*, 2021, **135**, 110235.

43 Y. Dong, H. Pang, H. Bin Yang, C. Guo, J. Shao, Y. Chi, C. M. Li and T. Yu, *Angew. Chem., Int. Ed.*, 2013, **52**, 7800–7804.

44 V. K. Tomer, N. Thangaraj, S. Gahlot and K. Kailasam, *Nanoscale*, 2016, **8**, 19794–19803.

45 Z. Li, L. Deng, I. A. Kinloch and R. J. Young, *Prog. Mater. Sci.*, 2023, **135**, 101089.

46 X. Wu, S. Li, B. Wang, J. Liu and M. Yu, *Renewable Energy*, 2020, **158**, 509–519.

47 M. Wang, Z. Bai, T. Yang, C. Nie, X. Xu, Y. Wang, J. Yang, S. Dou and N. Wang, *Adv. Energy Mater.*, 2022, **12**, 2201585.

48 P. Chen, Z. Wu, T. Guo, Y. Zhou, M. Liu, X. Xia, J. Sun, L. Lu, X. Ouyang, X. Wang, Y. Fu and J. Zhu, *Adv. Mater.*, 2021, **33**, 2007549.

49 G. S. Priyanga, G. Pransu and S. Sampath, *Chem. Phys. Impact*, 2024, **8**, 100408.

50 X. Ma, Y. Lv, J. Xu, Y. Liu, R. Zhang and Y. Zhu, *J. Phys. Chem. C*, 2012, **116**, 23485–23493.

51 R. Li, H. Peng, Q. Wu, X. Zhou, J. He, H. Shen, M. Yang and C. Li, *Angew. Chem., Int. Ed.*, 2020, **59**, 12129–12138.

52 Y. Yan, P. Zhang, Z. Qu, M. Tong, S. Zhao, Z. Li, M. Liu and Z. Lin, *Nano Lett.*, 2020, **20**, 7662–7669.

53 G. Wang, F. Li, D. Liu, D. Zheng, C. J. Abeggien, Y. Luo, X. Q. Yang, T. Ding and D. Qu, *Energy Storage Mater.*, 2020, **24**, 147–152.

54 H. Wu, H. Jiang, Y. Yang, C. Hou, H. Zhao, R. Xiao and H. Wang, *J. Mater. Chem. A*, 2020, **8**, 14498–14505.

This journal is © The Royal Society of Chemistry 2024

J. Mater. Chem. A, 2024, **12**, 15814–15828 | **15827**

55 M. A. Weret, C. F. J. Kuo, W. N. Su, T. S. Zeleke, C. J. Huang, N. A. Sahalie, T. A. Zegeye, Z. T. Wondimkun, F. W. Fenta, B. A. Jote, M. C. Tsai and B. J. Hwang, *J. Power Sources*, 2022, **541**, 231693.

56 J. F. Moulder, W. F. Stickle, P. E. Sobol and K. D. Bomben, *Handbook of X-Ray Photoelectron Spectroscopy*, 1992.

57 Y. Xu, Y. Wen, Y. Zhu, K. Gaskell, K. A. Cychosz, B. Eichhorn, K. Xu and C. Wang, *Adv. Funct. Mater.*, 2015, **25**, 4312–4320.

58 Y. Hu, A. Hu, J. Wang, X. Niu, M. Zhou, W. Chen, T. Lei, J. Huang, Y. Li, L. Xue, Y. Fan, X. Wang and J. Xiong, *J. Mater. Chem. A*, 2021, **9**, 9771–9779.

59 C. Zhao, B. Jiang, Y. Huang, X. Sun, M. Wang, Y. Zhang and N. Zhang, *Energy Environ. Sci.*, 2023, **16**, 5490–5499.

60 S. D. S. Fitch, G. E. Moehl, N. Meddings, S. Fop, S. Soulé, T. L. Lee, M. Kazemian, N. Garcia-Araez and A. L. Hector, *ACS Appl. Mater. Interfaces*, 2023, **15**, 39198–39210.

61 Z. Wang, J. Shen, J. Liu, X. Xu, Z. Liu, R. Hu, L. Yang, Y. Feng, J. Liu, Z. Shi, L. Ouyang, Y. Yu and M. Zhu, *Adv. Mater.*, 2019, **31**, 1902228.

62 C. Tian, P. Li, X. Hu, W. Yan, X. Xiang and L. Lu, *Small*, 2023, 2306928.

63 S. F. Ng, M. Y. L. Lau and W. J. Ong, *Adv. Mater.*, 2021, **33**, 2008654.

64 M. Zhang, W. Chen, L. Xue, Y. Jiao, T. Lei, J. Chu, J. Huang, C. Gong, C. Yan, Y. Yan, Y. Hu, X. Wang and J. Xiong, *Adv. Energy Mater.*, 2020, **10**, 1903008.

65 K. Liao, P. Mao, N. Li, M. Han, J. Yi, P. He, Y. Sun and H. Zhou, *J. Mater. Chem. A*, 2016, **4**, 5406–5409.

66 A. Manthiram, Y. Fu, S. H. Chung, C. Zu and Y. S. Su, *Chem. Rev.*, 2014, **114**, 11751–11787.

67 A. Hu, M. Zhou, T. Lei, Y. Hu, X. Du, C. Gong, C. Shu, J. Long, J. Zhu, W. Chen, X. Wang and J. Xiong, *Adv. Energy Mater.*, 2020, **10**, 2002180.

68 L. Ji, M. Rao, S. Aloni, L. Wang, E. J. Cairns and Y. Zhang, *Energy Environ. Sci.*, 2011, **4**, 5053–5059.

69 M. Liu, Q. Li, X. Qin, G. Liang, W. Han, D. Zhou, Y. B. He, B. Li and F. Kang, *Small*, 2017, **13**, 1602539.

70 Y. Chen, T. Wang, H. Tian, D. Su, Q. Zhang and G. Wang, *Adv. Mater.*, 2021, **33**, 2003666.

71 S. J. Kim, Y. Jeoun, J. Park, S. H. Yu and Y. E. Sung, *Nanoscale*, 2020, **12**, 15466–15472.

72 J. Shen, X. Xu, J. Liu, Z. Liu, F. Li, R. Hu, J. Liu, X. Hou, Y. Feng, Y. Yu and M. Zhu, *ACS Nano*, 2019, **13**, 8986–8996.

73 L. Ding, Q. Lu, A. D. C. Permana, S. Oswald, M. Hantusch, K. Nielsch and D. Mikhailova, *Energy Technol.*, 2021, **9**, 2001057.

74 Y. Xie, J. Ao, L. Zhang, Y. Shao, H. Zhang, S. Cheng and X. Wang, *Chem. Eng. J.*, 2023, **451**, 139017.

75 D. Wang, K. Ma, J. Hao, W. Zhang, C. Wang, C. Xu, H. Shi, Z. Ji, X. Yan and Y. Gu, *Nano Energy*, 2021, **89**, 106426.

76 H. Zhang, Q. Liu, S. Ruan, C. Ma, X. Jia, W. Qiao, L. Ling and J. Wang, *Appl. Surf. Sci.*, 2022, **578**, 152022.

77 Y. Hu, W. Chen, T. Lei, Y. Jiao, J. Huang, A. Hu, C. Gong, C. Yan, X. Wang and J. Xiong, *Adv. Energy Mater.*, 2020, **10**, 2000082.

78 L. Shi, S. M. Bak, Z. Shadike, C. Wang, C. Niu, P. Northrup, H. Lee, A. Y. Baranovskiy, C. S. Anderson, J. Qin, S. Feng, X. Ren, D. Liu, X. Q. Yang, F. Gao, D. Lu, J. Xiao and J. Liu, *Energy Environ. Sci.*, 2020, **13**, 3620–3632.

79 S. Dörfler, H. Althues, P. Härtel, T. Abendroth, B. Schumm and S. Kaskel, *Joule*, 2020, **4**, 539–554.

80 D. Qu, G. Wang, J. Kafle, J. Harris, L. Crain, Z. Jin, D. Zheng, D. Qu, G. Wang, J. Kafle, J. Harris, L. Crain, D. Zheng and Z. Jin, *Small Methods*, 2018, **2**, 1700342.

81 J. T. Kim, A. Rao, H. Y. Nie, Y. Hu, W. Li, F. Zhao, S. Deng, X. Hao, J. Fu, J. Luo, H. Duan, C. Wang, C. V. Singh and X. Sun, *Nat. Commun.*, 2023, **14**, 1–10.

82 T. Pakki, E. H. Mohan, N. Y. Hebalkar, J. Adduru, S. V. Bulusu, A. Srinivasan, K. M. Mantravadi and N. R. Tata, *J. Mater. Sci.*, 2019, **54**, 9075–9087.

83 R. Li, Y. Zeng, L. Song, J. Lv, C. Wang, C. Zhou, S. Cai, T. Chen, S. Yue, K. Ma and H. Yue, *Small*, 2023, 2305283.

84 S. S. Zhang, *J. Electrochem. Soc.*, 2012, **159**, A920–A923.

85 Y. Diao, K. Xie, S. Xiong and X. Hong, *J. Electrochem. Soc.*, 2012, **159**, A1816–A1821.

86 S. Ponnada, M. S. Kiai, D. B. Gorle and A. Nowduri, *Nanoscale Adv.*, 2021, **3**, 4492–4501.

87 X. Gao, C. Zheng, Y. Shao, V. R. Shah, S. Jin, J. Suntivich and Y. L. Joo, *ACS Appl. Mater. Interfaces*, 2023, **15**, 19011–19020.

88 Y. Hu, W. Chen, T. Lei, Y. Jiao, J. Huang, A. Hu, C. Gong, C. Yan, X. Wang and J. Xiong, *Adv. Energy Mater.*, 2020, **10**, 2000082.

89 H. Pan, K. S. Han, M. H. Engelhard, R. Cao, J. Chen, J.-G. Zhang, K. T. Mueller, Y. Shao, J. Liu, H. Pan, K. S. Han, R. Cao, J. Chen, J.-G. Zhang, K. T. Mueller, Y. Shao, J. Liu and M. H. Engelhard, *Adv. Funct. Mater.*, 2018, **28**, 1707234.

90 Z. Meng, S. Li, H. Ying, X. Xu, X. Zhu, W.-Q. Han, Z. Meng, H. Ying, X. Xu, X. Zhu, S. Li and Q. W. Han, *Adv. Mater. Interfaces*, 2017, **4**, 1601195.

15828 | *J. Mater. Chem. A*, 2024, **12**, 15814–15828

This journal is © The Royal Society of Chemistry 2024